nature communications

Article

https://doi.org/10.1038/s41467-024-54227-9

Crystallinity of covalent organic frameworks controls immune responses

Received: 11 September 2023

Accepted: 4 November 2024

Published online: 11 November 2024

Check for updates

Arezoo Esrafili[1,7], Abhirami Thumsi[2,7], Madhan Mohan Chandra Sekhar Jaggarapu[3], Richard G. Nile[1], Joshua Kupfer[1], Margaret Dugoni[4], Abhirami P. Suresh[2], Taravat Khodaei[3], Huikang Qian[3], Anna Mathis[3], Brandon Kim[3], Srivatsan J. Swaminathan[5], Wei Sun[3], Yeo Weon Seo[3], Kelly Lintecum[4], Sanmoy Pathak[3], Xinbo Tong[1], Julianne L. Holloway[1], Kailong Jin[1] & Abhinav P. Acharya[2,3,6]

Biomaterials can act as pro- or anti-inflammatory agents. However, effects of biomaterials crystallinity on immune responses are poorly understood. We demonstrate that the adjuvant-like behaviour of covalent organic framework (COF) biomaterial is dependent on its crystallinity. COF crystallinity is inversely correlated with the activation of mouse and human dendritic cells (DC), but with antigen presentation by mouse DCs only. Amorphous COFs upregulates NFkB, TNF, and RIG-I signalling pathways, as well as the chemotaxis-associated gene *Unc5c*, when compared to crystalline COFs. Meanwhile, *Unc5c* inhibition disrupts the correlation between crystallinity and DC activation. Furthermore, COFs with the lowest crystallinity admixed with chicken ovalbumin (OVA) antigen prevent OVA-expressing B16F10 tumour growth in 60% of mice, with this protection associated with the induction of antigen-specific, pro-inflammatory T cell. The lowest crystalline COFs admixed with TRP2 antigen can also prevent non-immunogenic YUMM1.1 tumour growth in 50% of mice. These findings demonstrate that the crystallinity of biomaterials is an important aspect to consider when designing immunotherapy for pro- or anti-inflammatory applications.

Recent years have witnessed significant advances in nanomaterial-based immunotherapy design[1–5], resulting in the development of highly effective and clinically relevant therapies[6–8]. Nanomaterials, including inorganic nanoparticles (NP) (silica NP, metal NP, carbon nanotubes, etc.) and organic and biomolecules-based NPs (micelles, liposome, nanogel, polymer, etc.) have demonstrated tremendous promise in a range of applications[9–13]. For example, encapsulation of antigens in biodegradable and biocompatible polymers such as Poly (lactic-co-glycolic acid) (PLGA) is widely used as an approach in vaccine and drug delivery systems[14]. In addition, cationic liposomes used both for encapsulating antigens and as coating polymers to prevent immune recognition, have been approved for treating meningitis, infection, and cancer[15]. Among different nanomaterials, 2D nanomaterials have great potential in impacting biomedical applications due to their unique characteristic of high surface area compared to 1D or 3D nanomaterials. The high surface area provides several anchoring sites, resulting in high interactions of 2D nanomaterials with cellular components and biomolecules. The ease of synthesis and

[1]Chemical Engineering, School for the Engineering of Matter, Transport, and Energy, Arizona State University, Tempe, AZ, USA. [2]Department of Pathology, School of Medicine, Case Western Reserve University, Ohio, OH, USA. [3]Department of Biomedical Engineering, Case Western Reserve University, Ohio, OH, USA. [4]Biomedical Engineering, School of Biological and Health Systems Engineering, Arizona State University, Tempe, AZ, USA. [5]School of Life Sciences, Arizona State University, Tempe, AZ, USA. [6]Case Comprehensive Cancer Centre, Case Western Reserve University, Ohio, OH, USA. [7]These authors contributed equally: Arezoo Esrafili, Abhirami Thumsi. e-mail: axa1826@case.edu

functionalization of 2D nanomaterials is another desirable property that increases their use in biomedical applications. Surface properties, size, and geometry of 2D nanomaterials have a critical role in cellular interaction as well[16–18]. In general, there are two models of the interaction of 2D nanomaterials with cells: orthogonal and parallel attachment models. Orthogonal attachment includes the hydrophobic attraction of lipid tails in the cell membrane and nanomaterial surface[16]. In the second mechanism (parallel attachment mode), the primary driving force is the hydrophilic attraction of cell membranes with 2D nanomaterial surfaces[16]. These interactions can also play an important role in determining functional responses from dendritic cells, as they interact with 2D materials such as covalent organic frameworks (COF).

COFs are crystalline polymers that have made significant advances in the field of drug delivery and theranostic application[19–23]. Highly ordered and porous structures of COFs make them an ideal carrier for drug loading, while their chemical stability makes them effective for target delivery and controlled release of drugs and for theranostic applications[24,25]. COFs have also been used to deliver immunoactive molecules such as poly(I:C) and CpG to modulate tumour growth in murine models[21,23]. In addition to the inherent properties imparted by chemical constitutions, physicochemical properties play a significant role in redefining the functionality of nanomaterials as immunoactive materials. For example, studies have shown that nanoparticles smaller than 25 nm travel through the lymphatic system more efficiently compared to larger particles (approximately 100 nm in diameter), resulting in a higher accumulation in lymph node-resident DCs[26]. In addition to the size, other physical properties like crystallinity of nanomaterials, may also be manipulated to achieve therapeutic benefits.

Crystalline aluminium hydroxide (AH), non-crystalline aluminium phosphate adjuvant (AP), and Imject™ Alum composed of amorphous aluminium hydroxycarbonate, and crystalline magnesium hydroxide are extensively used in the clinic and pre-clinical research as adjuvants[27–29]. Studies have reported that crystalline materials like aluminium salts, monosodium urate (MSU), and silica crystals can activate antigen-presenting cells via the activation of nucleotide-binding domain (NOD)-like receptor protein 3 (NLRP3) pathway[30,31]. In contrast, it was also demonstrated that amorphous alum particles led to increased activation of DCs compared to crystalline alum particles[32].

Biomaterial-based adjuvants are being used to generate vaccines to cause either pro- or anti-inflammatory responses in cancer or autoimmune disorders, respectively. For instance, it is understood that adjuvants containing aluminium (alum) predominantly trigger Th2-type humoral immunity by inducing the production of interleukin 4 (IL-4)[27,28]. Although Th2 immune response protects against pathogens, Th1 immune response is required to activate macrophages and generate cytotoxic T cells (CTL) against diseases like cancer. Microcrystalline tyrosine (MCT), a crystal form of amino acid, has been used as an adjuvant[33] leads to activation of the NLRP3 inflammasome in a caspase-dependent manner and leads to secretion of IL-1beta, independent of TLR signalling, and induces less IL-4 and immunoglobulin E (IgE) formation compared to alum[34]. Despite significant advances in vaccine immunotherapy, it remains unclear whether the degree of crystallinity of biomaterials skews the immune system towards pro- or anti-inflammatory responses. Additionally, due to the conflicting reports on the role of crystalline materials in modulating immune responses, in this report, the role of crystallinity in modulating immune responses was studied.

It is important to note that materials have a smooth gradient from crystalline to amorphous in the body, however, during tissue damage abrupt break in gradients are generated in the form of uric acid metabolite-based crystals[32,35–38]. It is not well understood if this abrupt change in crystallinity modulates immune responses and if the crystalline properties can be utilized for skewing immune responses. Unfortunately, studying the effect of gradients of crystallinity is highly challenging, because finely controlling the crystallinity of biomaterials is not trivial[39].

COFs, a new class of biomaterials, whose structures can be controlled at the molecular scale, and thus the degree of the crystallinity of these materials can be precisely controlled[40–46]. Therefore, in this report, COFs were generated with controlled crystallinity to assess the role of crystallinity on immune responses. The crystallinity of 2D COF is controlled by in-plane direction covalent bonds and out-of-plane noncovalent bonds. To ensure that well-organized and crystalline 2D COF is generated, it is crucial to regulate lateral growth of organic subunits via covalent bonds and vertical stacking of layers via non-covalent interactions[47]. Different linkages, solvent ratio, temperature, and self-assembly/self-complementary monomers may regulate the crystallinity of COFs[48].

In this study, we demonstrate that amorphous COF leads to the activation of both human and mouse DCs and upregulate the *TNF* and *NFKB* signalling pathways compared to COF with higher crystallinity. Additionally, amorphous COF with OVA as an antigen model effectively inhibit tumour growth in mice bearing OVA-expressing B16F10 tumours and enhance OVA-specific immune responses. These findings suggest that modulating the crystallinity of COFs could serve as a powerful strategy for designing biomaterials that regulate immune responses. This strategy offers significant potential for developing vaccine immunotherapy.

Results

Synthesis and characterization of different crystallinities of COFs

In this investigation, methods were developed to control the crystallinity of TAPB (1,3,5-tris(4-aminophenyl) benzene)-PDA (terephthalaldehyde) COF materials (Fig. 1a). The optimal crystal growth of COF as established by varying reaction times. In this study, linkage, solvent ratio, and temperature were kept constant, while a structural-dependent approach via modulation of reaction time control was used to control the degree of crystallinity. This facile approach includes pi-pi stacking and H bonding between layers (out-of-plane) and interaction between building blocks and functional groups (in-plane) during polymerization (Fig. 1a) provides variable crystallinity as the assembly of 2D COFs grows.

COF samples with different degrees of crystallinity were formed with reaction times of 15 s, 60 s, 10 min, 1 h, and 3 days (noted as COF1, COF2, COF3, COF4, and COF5, respectively). At 3 days reaction time, the highest crystallinity and porous imine-linkage COF was achieved through strong interaction between the 2D sheets with long-range organization and order (Fig. 1a). Powder X-ray diffraction (PXRD) was used to confirm the crystallinity of the generated COFs. Diffraction peaks of COF5 (COF with the highest crystallinity) at 2.88°, 5°, 5.7°, and 7.5°, respectively assigned to ⟨100⟩, ⟨110⟩, ⟨200⟩, and ⟨210⟩ reflection, confirmed polycondensation of 1,3,5-Tris(4-aminophenyl) benzene (TAPB) and Terephthalaldehyde (PDA) monomers (Fig. 1b). These data demonstrated that using different reaction times, various degrees of crystallinity was obtained (COF1, COF2, COF3, COF4, COF5; lowest to highest crystallinity). The data from DLS shows that the suspended COF particles in deionized water have aggregated into cluster of 1–2 μm (hydrodynamic diameter) (Fig. 1c, Supplementary Fig. 1a). The Fourier-transform infrared (FT-IR) was performed to confirm formation of the C=N stretching of imine bonds at 1640–1690 cm^{-1} (Fig. 1d). The size of the as-obtained COF particles was determined using scanning electron microscopy (SEM) and dynamic light scattering (DLS), and it was measured as ~200 nm in diameter the lowest crystallinity, medium crystallinity, the highest crystallinity) (Fig. 1e).

DCs are capable of phagocytosing COFs

The degree of crystallinity of COFs, controlled by varying the reaction time, can lead to variable immune responses, which was investigated in

https://doi.org/10.1038/s41467-024-54227-9

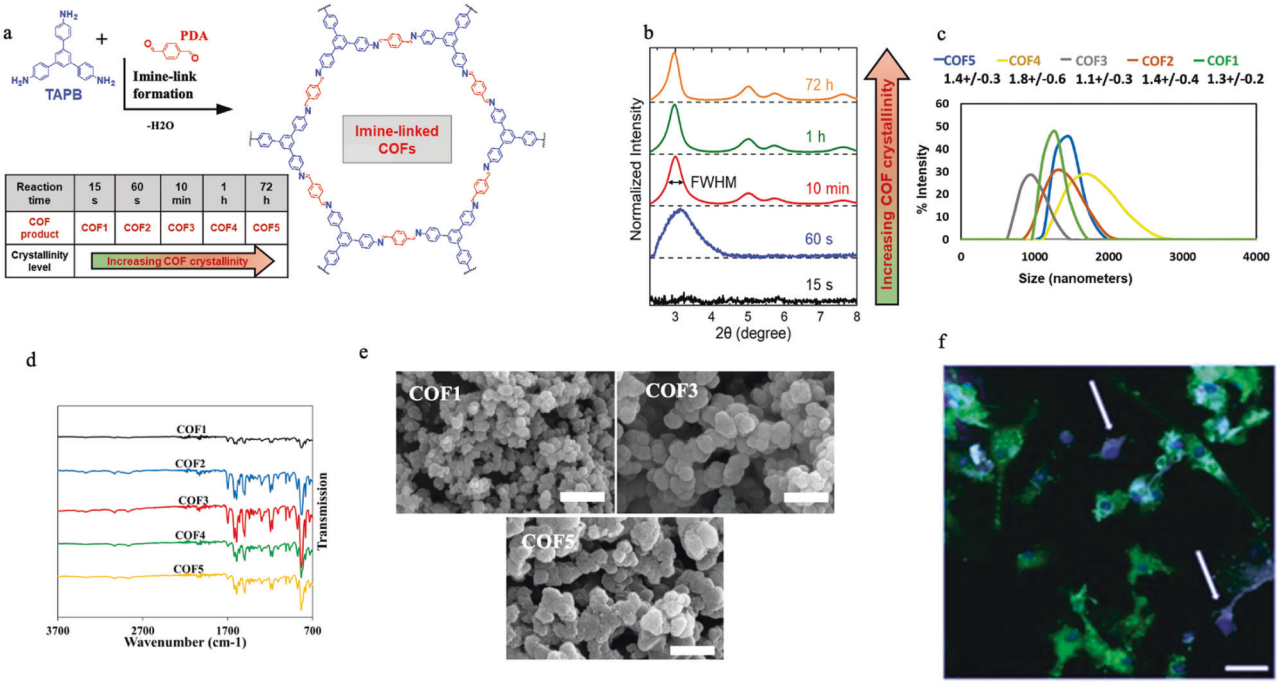

Fig. 1 | COF characterization. a COF reaction scheme, condensation reaction between terephthalaldehyde and trifunctional tris(4-aminophenyl) benzene to form a 2D imine-linked COF. **b** PXRD spectra of different crystallinity of COFs. **c** DLS graphs of different crystallinity of COFs (**d**) FT-IR of COFs. **e** SEM images of TAPB-PDA COF particles with low (COF1), medium (COF3), and high (COF5) crystallinity, Scale bar = 1 μm, Representive SEM images of COF ($n = 3$). **f** A representative confocal image of DCs treated with COF1, green = cytosol, magenta = COF1, blue = nucleus, Scale bar = 25 μm. The arrow in the image indicates COFs, stained with RBITC, being phagocytosed by DCs.

this study. DCs were chosen to test the effect of the degree of crystallinity because these are natural scavengers of foreign entities in the body. Moreover, DCs also form the bridge between innate and adaptive immunity and are responsible for generating vaccine responses to foreign biomaterials. To test the capability of DCs derived from bone marrow of mice to phagocytose COFs, confocal microscopy was utilized and the result shows that DCs can phagocytose COFs of variable crystallinity. Briefly, DC's membrane was stained with 1,1-Dioctadecyl-3,3,3,3-tetramethylindodicarbocyanine (DiD), COFs were labelled by rhodamine B isothiocyanate (RBITC), the nucleus was stained with DAPI, and cytochalasin D used to inhibit the phagocytosis (Fig. 1f, Supplementary Fig. 1b).

Varying degrees of COF crystallinity generate different immune responses in vitro

To investigate if the degree of crystallinity of COFs can generate variable immune responses, bone marrow-derived dendritic cells isolated from 6–8 weeks old C57BL/6j were treated with COFs of different crystallinity pre-mixed with the model antigen protein ovalbumin (OVA). Lipopolysaccharide (LPS) was also added as a mimic to inflammation. Notably, COF1 (lowest crystallinity) with OVA in the presence of LPS was able to increase activation of DCs, which was determined by analysis of geometric mean fluorescent intensity (gMFI) $CD86^+$, (a co-stimulatory molecule), 1.44-fold higher than COF5 (highest crystallinity) with OVA (Fig. 2a). Interestingly, degree of crystallinity of COF affects anti-inflammatory responses differently as well. $COF1^+$OVA treated DCs had decreased gMFI of $CD163^+$ compared to LPS, soluble OVA, and COF5 with OVA (with and without LPS, Fig. 2b, Supplementary Fig. 3b). However, DCs in presence of $COF1^+$OVA (with and without LPS) expressed higher levels of CD206 (Fig. 2c, Supplementary Fig. 3c). Significantly higher gMFI for H2-kb SIINFEKL peptide bound MHCI was observed in DCs treated with COF^+OVA (with and without LPS) compared to other treatments including COF5 (2650-fold higher than $COF5)^+$OVA and soluble OVA (2.3-fold higher than soluble OVA) (Fig. 2d, Supplementary Fig. 3d). Intracellular cytokine staining was also performed on the DCs treated with different COFs. It was observed that IL-12p70 expression in DCs, which is T-helper type 1 polarizing cytokine, is significantly reduced in the presence of $COF5^+$OVA with LPS condition compared to all the other COFs tested. Moreover, IL-10 expression in DCs, an anti-inflammation-driving cytokine, was variable between the groups, and there was no correlation between the COFs (Supplementary Fig. 4a, b). Overall, these data suggest that although no direct correlation is observed between the crystallinity of COFs and pro-inflammatory cytokine expression by DCs, data indicates that the highest crystalline COF might be less inflammatory.

To investigate if COFs modulated DCs due to the presence of endotoxins, a chromogenic endotoxin kit was used. The result reveals that the COF endotoxin levels are below the detection limit of 0.1 endotoxin unit ml^{-1}, and thus, COFs do not activate DCs due to endotoxin presence (Supplementary Fig. 5a). To evaluate the cytotoxic effect of COFs, live/dead staining (Viability Dye 780) and analyses via flow cytometry was performed. When cells undergo apoptosis (a late stage of cell death), the Viability Dye 780 penetrates the cells through plasma membrane integrity and irreversibly binds to the cell surface and intracellular amines, generating a significantly more intense fluorescence signal. The percentage of live cells is calculated by dividing the number of unstained (viable) cells by the total number of cells (both unstained and stained) and multiplying the result by 100. This will give the percentage of cells that are alive. The result demonstrated no significant differences in the percentage of viable COF-treated DCs at 0.05 mg ml-1 compared to no treatment cells (Supplementary Fig. 5b). Cytotoxicity of COFs on NIH3T3 fibroblast cell lines was also performed. These cells were cultured and then exposed to two different COF concentrations. The cytotoxic effects on NIH3T3 mouse fibroblast cells were assessed using the PicoGreen

https://doi.org/10.1038/s41467-024-54227-9

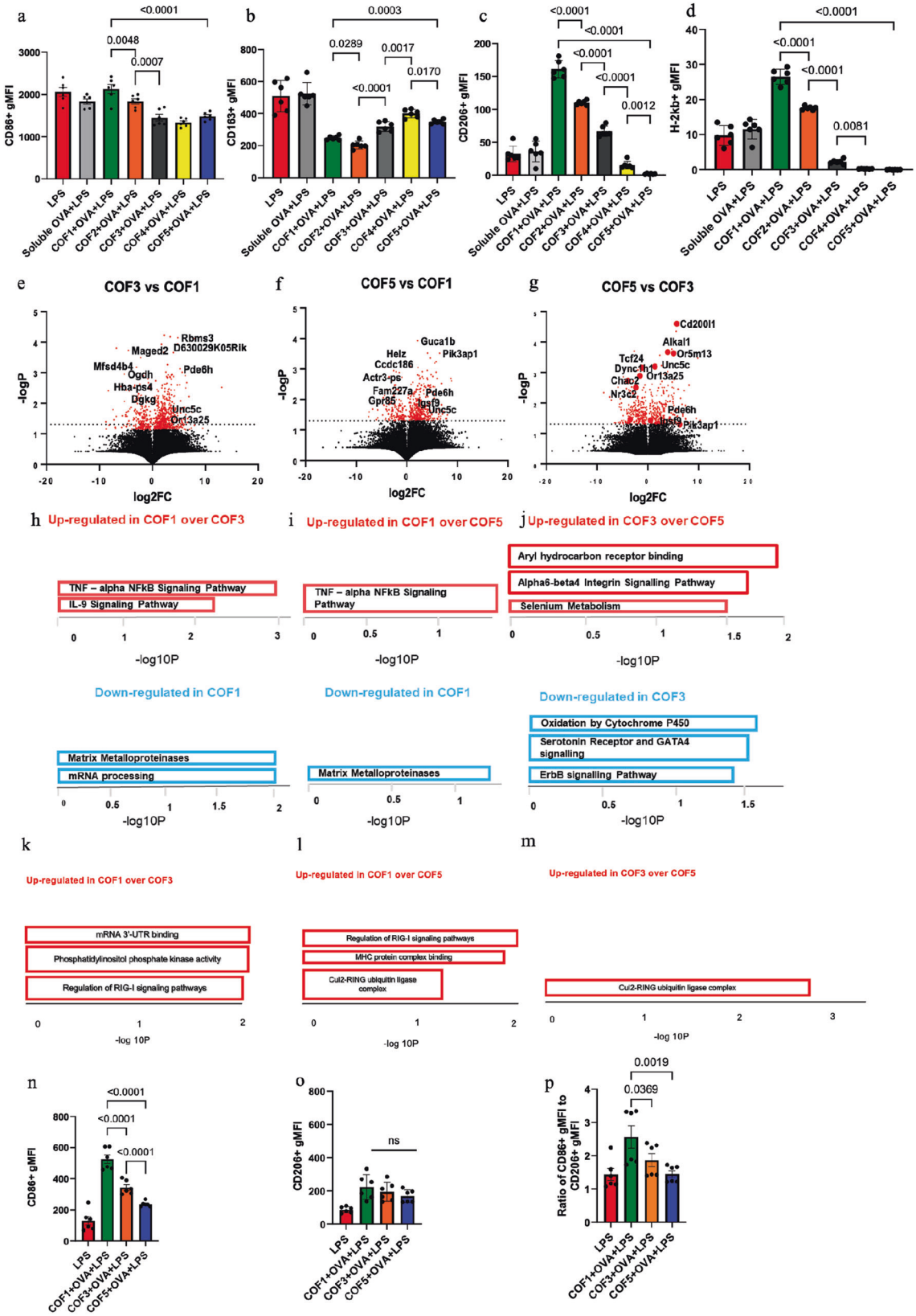

assay, following the procedure described in the methods section. The result showed no significant difference in DNA concentration (ng/ml) of NIH3T3 cells treated with COFs and no treatment. This assay allows us to understand the impact of COFs on the overall cell population, meaning that COFs do not have a negative effect on NIH3T3 cell proliferation (Supplementary Fig. 5c).

Role of *Unc5c* gene in the activation of DCs in presence of COFs in vitro

To identify the signalling pathways that were modified due to the exposure to different degrees of crystallinity of COFs, bulk RNA-sequencing was performed on COF-treated bone marrow-derived DCs. The data from RNA-seq experiment was analysed for gene

Fig. 2 | Activation of mice and human DCs in the presence of COFs and RNA-seq dataset. a In the presence of LPS, mouse DCs treated with COF1 with OVA expressed higher CD86 + , in vitro (mean ± s.d, $n = 6$ technical replicate; one-way ANOVA test). **b** DCs treated with COF1 with OVA had lower gMFI CD163+ in CD11c+ compared to other treatments, with inflammation, in vitro (mean ± s.d, $n = 6$ technical replicate; one-way ANOVA test). **c** High expression of CD206+ in CD11c+ in presence of COF1 with OVA compared to COF 5 with OVA, LPS, and soluble OVA, in vitro (mean ± s.d, $n = 6$ technical replicate; one-way ANOVA test). **d** COF 1 with OVA increase cross-presentation of 257–264 SIINFEKL OVA peptide in DC, with inflammation, in vitro (mean ± s.d, $n = 6$ technical replicate; one-way ANOVA test). **e** Volcano plot of COF3 vs COF1, $n = 3$ biological replicate; one-way ANOVA test. COF1. **f** Volcano plot of COF5 vs. COF1, $n = 3$; one-way ANOVA test. **g** Volcano plot of COF5 vs. COF3, $n = 3$; one-way ANOVA test. **h**–**j** WikiPathways of COF3 vs. COF1, COF5 vs. COF1, COF3 vs. COF5 respectively, $n = 3$; one-way ANOVA test. **k**–**m** Gene Ontology (GO) analysis of COF3 vs. COF1, COF5 vs. COF1, COF3 vs. COF5 respectively, $n = 3$ biological replicate; one-way ANOVA test. **n** Higher expression of CD86+ in human dendritic cells treated with COF1 compared to COF5 (in presence of soluble OVA and LPS, mean ± s.d, $n = 6$ biological replicate; one-way ANOVA test). **o** COF1 with LPS and soluble OVA can upregulate expression of CD206+ (mean ± s.d, $n = 6$ biological replicate; one-way ANOVA test). **p** An increase of the ratio of CD86+ gMFI to CD206+ gMFI in COF1 with ova compared to COF5 (mean ± s.d, $n = 6$ biological replicate; one-way ANOVA test). All significant differences are not shown for clarity.

expression profiles and molecular mechanisms underlying the response of DCs to COF treatment. Volcano plots of RNA-seq on COFs treated DCs were generated to evaluate the specific RNA changes in treated DCs (Fig. 2e, f, g). Notably, genes dependent on the degree of crystallinity were identified by comparing gene expressions between COF1 and COF3, COF1 and COF5, and COF3 and COF5. It was observed that the expression of two genes, *Pde6h* and *Unc5c*, decreased with increasing crystallinity. It was observed that there was an upregulation of *Pde6h* gene (log2 fold change: 5.2, *P*-value: 7e-4) and *Unc5c* gene (log2 fold change: 2.22, *P*-value: 3.3e-2) in COF1 treated DCs compared to COF3 (Fig. 2e). Cyclic nucleotide phosphodiesterase (PDE) can degrade and remove Cyclic adenosine monophosphate (cAMP). Increased cAMP, via cAMP-dependent protein kinase (PKA), decreases the release of pro-inflammatory cytokines (IL-12 and *TNF*), increases the production of anti-inflammatory cytokine (IL-10), and may impair the capacity of DCs to prime pro-inflammatory T cells (Th1) differentiation. Hence, increased cAMP in DCs can potentially treat inflammatory diseases like asthma[49,50]. Furthermore, several studies have demonstrated that *Unc5c* expression, a netrin receptor, can be associated with cellular movement and is either lost or significantly reduced in some cancers, including colorectal cancer (CRC), at the messenger RNA (mRNA) level[51]. However, the role of *Unc5c* in DCs is unknown and may play an important role in cell movement[52]. Comparing COF1 vs. COF5 treatment demonstrated an upregulation of *Guca1b* gene (log2 fold change: 2.09, *P*-value: 1.2e-4), *Pik3ap1* gene (log2 fold change: 6.46, *P*-value: 3e-4), *Pde6h* gene (log2 fold change: 1.74, *P*-value: 5e-3), and *Unc5c* gene (log2 fold change: 3.61, *P*-value: 2e-2, Fig. 2f). Significant upregulation of same genes (*Unc5c* with log2 fold change: 1.38, *P*-value: 6.5e-4) in COF3 treated DCs was observed compared to COF5 (Fig. 2g). In addition, Volcano plots of no treatment (control) vs. COFs were evaluated as well (Supplementary Fig. 6).

It was observed that there is an upregulation of gene sets that encoded nuclear factor kappa B (*NFkB)* signalling pathways (WikiPathways) that regulate pro-inflammatory cytokine, tumour necrosis factor alpha (*TNF)*, in DCs treated with COF1 compared to COF3 (Fig. 2h). Consequently, COF1 treated DCs produce more *TNF* than COF3 treated DCs. Moreover, genes associated with matrix metalloproteinases (MMP) pathways are downregulated in COF1 compared to COF3 and COF5 (Fig. 2h, i). In addition to extracellular matrix degradation, MMPs also participate in various cellular processes like cell migration, proliferation, differentiation, apoptosis, cytokine activation, and immune cell modulation. Moreover, it has been demonstrated that inflammatory cytokines, such as transforming growth factor-beta (TGF-β) and interleukin-10 (IL-10), can inhibit MMP production and activity. These anti-inflammatory cytokines can suppress MMP expression, thereby reducing the excessive degradation of ECM components[53]. DCs treated with COF3 also upregulated genes associated with integrin pathways and selenium metabolism and downregulated oxidation, GATA4 signalling, and ErbB pathway as compared to COF5 (Fig. 2j). Selenium may regulate the immune function of mouse DCs through the ROS- and selenoprotein K (SELENOK)-mediated ERK, Akt and RhoA/ROCK signalling. A selenium deficiency was found to enhance the migration of immature dendritic cells (imDC), but it significantly inhibited their ability to phagocytose antigens. Conversely, elevated selenium levels hindered the migration ability of imDCs without affecting their phagocytic capacity[54]. Additionally, there is upregulation of aryl hydrocarbon receptor (AhR) in DCs treated with COF3 as compared to COF5 (Fig. 2j). Th17 cells and dendritic cells express high levels of AhR. AhR-induced CYP1A1 can be suppressed by *NFkB* activators such as the inflammatory cytokines IL-1b, IL-6, and *TNF*[55]. Our pathway's result indicated a downregulation of cytochrome P450 in COF3-treated DCs compared to COF5, which can be relevant to *TNF* cytokine.

To test if the crystalline COFs directly affect maintaining human DC activation, human peripheral blood dendritic cells were treated with COFs with variable crystallinity. Briefly, the monocytes were obtained after performing a Ficoll gradient from 6 individual sources, and peripheral blood mononuclear cells were isolated using a $CD14^+$ magnetic cell separation. Isolated $CD14^+$ monocytes were differentiated into immature monocyte-derived dendritic cells in 7 days by culturing with human GM-CSF and IL-4. The result shows that human DCs treated with COF1 with LPS, and soluble OVA express higher CD86 gMFI compared to cells treated with COF5 with LPS and soluble OVA (2.25-fold higher than COF5) (Fig. 2n). Moreover, human DCs in presence of COF1 with OVA and LPS expressed higher CD206 gMFI compared to cells treated with COF5 with LPS and soluble OVA, 1.8-fold higher than COF5 (Fig. 2o). Finally, a significant increase in the ratio of $CD86^+$ gMFI to $CD206^+$ gMFI was observed in COF1 with OVA and LPS treatment group (Fig. 2p). These data demonstrated that the amorphous COF was able to maintain pro-inflammatory DC phenotype in both murine and human DCs. It is important to note that only significant differences between COF1 and COF2, COF2 and COF3, COF4, and COF5, and COF1 and COF5 are shown in Fig. 2a–d and Fig. 2n–p to make the Fig. 2 simple and understandable. For example, there is also a significant difference in $CD86^+$ gMFI between DCs treated with COF1 with OVA and LPS and soluble OVA with LPS. Significant differences in $CD86^+$ gMFI were observed when DCs were treated with COF1 with OVA and LPS and, COF3 with OVA and LPS, and COF4 with OVA and LPS. Significant differences in $CD163^+$ gMFI between DCs treated with COF1 with OVA and LPS and COF3 with OVA and LPS, and COF4 with OVA and LPS were observed.

To test if different biomaterials with variable crystallinity also influence DC function, Poly (l-lactic Acid) (PLLA) film with different crystallinity was synthesized. To obtain PLLA films with different levels of crystallinity, the as-obtained PLLA films were first thermally annealed at 210 °C for 10 min to reach a completely amorphous melt state, then quenched to 105 °C, and finally held to undergo isothermal crystallisation for controlled amounts of time. Completely amorphous PLLA films were also obtained by thermally quenching them from 210 °C to room temperature, without the above-mentioned isothermal annealing step. Using this approach, the degrees of crystallinity of PLLA were obtained in a wide range, from 0 to 52.2% with 0% representing completely amorphous films[56]. The varying degrees of

crystallinity in these PLLA samples were confirmed using both differential scanning calorimetry (DSC) and X-ray diffraction (XRD), where DSC measures crystallinity by monitoring the enthalpy of melting crystals and XRD measures crystallinity by calculating the ratio between the area of the deconvoluted crystalline peaks and the total area of the crystalline and amorphous peaks[57,58].

To understand the effect of DCs when cultured on PLLA films with different crystallinity flow cytometry was employed. The results demonstrated that DCs treated with amorphous PLLA show higher expression of CD86 compared to the highest crystallinity of PLLA (Supplementary Fig. 7a). There was no specific trend observed in the expression of CD163 and CD206 when DCs were treated with different crystallinity of the PLLA film (Supplementary Fig. 7b, c). Overall, we found that similar to amorphous COFs, amorphous PLLA film is able to activate DCs and induce higher expression of $CD86^+$ compared to the higher crystallinity material. Some of the differences observed in COFs were not observed in PLLA, potentially due to the lower range of crystallinity in PLLA films.

To further understand the relationship between crystallinity and the function of DCs, the role of *Unc5c* gene, which best correlated with crystallinity, was investigated. *Unc5c* has been implicated in modulating microtubule function, which is essential for migration and intracellular transport[59,60]. Thus, *Unc5c* might play an important role in the intracellular transport of COFs and, thus, might modulate the activation phenotype of DCs. To test this, we cultured bone marrow-derived dendritic cells with siRNA against *Unc5c* for 72 h and then added COFs and LPS to the culture for 2 h. After 24 h of further culture with internalized COFs, flow cytometry was performed to determine the activation phenotype of DCs. We found no significant difference in the percentage of CD86, CD206, and CD163 when DCs treated with LPS and, COFs with LPS in the presence of siRNA silencing *Unc5c* gene. Moreover, there is a significant decrease in expression of CD86, CD206, and CD163 when DCs treated with COFs with LPS in the presence of siRNA silencing *Unc5c* gene compared to LPS and non-specific siRNA (Fig. 3a–c). Another set of experiment with different batches of COFs and a different bone marrow-derived DCs was performed to support the gene silencing result. No significant difference in CD86 mean fluorescence intensity (MFI), CD206 MFI, and CD163 MFI when DCs were treated with COFs in the presence of siRNA silencing *Unc5c* gene was observed (Supplementary Fig. 8a–c). The results show the critical role of *Unc5c* in the activation of DCs in the presence of COFs. It was also observed that COF1 upregulated H-2kb, which suggests higher expression of the MHC peptide complex. To probe the mechanism for this increase in expression, quantitative COF internalization by bone marrow-derived DCs was performed. COFs were labelled with Fluorescein isothiocyanate (FITC) and then cultured with DCs for 2 h, and the internalization was quantified using flow cytometry. The result showed that the amount of amorphous COF (COF1) that can be internalized by DCs is significantly higher than the amount of the highest crystallinity of COF (COF5), which strongly influences the efficacy of cross-presentation of OVA peptide on MHC I (Supplementary Fig. 8d). Figure 3d shows the possible overall mechanisms that might be involved in crystallinity-mediated DC activation. As shown in Fig. 2k–m (gene ontology analysis), there is up-regulation of the retinoic acid-inducible gene (*RIG-I*) signalling pathway in DCs treated with COF1 (amorphous) compared to COF3 and COF5. This study found that amorphous COFs upregulated *NFkB* signalling pathway, and downstream CD86 expression on DCs. These results are supported by studies which show that *RIG-I* signalling pathway activates *NFkB* signalling[61,62]. In addition, it has been reported that *RIG-I* signalling enhances the process of phagocytosis in peripheral blood mononuclear cells (PBMC)[63]. In this study also, higher phagocytosis of the amorphous COF was observed, in tandem with increased *RIG-I* signalling (Supplementary Fig. 8d). Moreover, it was reported that *Unc5c* has a significant role in the stabilisation and assembly of microtubules in neurons[59,60]. In addition, microtubules also play an important role in phagocytosis by DCs[64]. Although the role of *Unc5c* and microtubule assembly in DCs has not been previously reported, in this report we observed *Unc5c* upregulation and increased phagocytosis by DCs of amorphous COFs. Therefore, upregulation of *Unc5c* in DCs treated with COF1 can influence the transport of vehicles, including phagosome and lysosomes along microtubules in the cytoplasm and the process of OVA peptide loading onto MHC I and ultimately may enhance activation of cytotoxic T cells (Fig. 3d).

Different COF crystallinities induce different immune cell recruitment at injection sites

We tested the mechanism of action in vitro, however, these mechanisms will translate in vivo if the COFs are able to accumulate DCs at the injection site. Therefore, COF1, COF2, COF3, COF4, and COF5 were injected at different sites in the same mice (to correct for inter-mouse variability). These injection sites were isolated after 24 h, and flow cytometry was employed to determine the type of cells infiltrating the injection site. All the data from flow cytometry for each COF from 6 mice was pooled together to determine differences between the COFs. It was observed that the COFs could attract DCs, macrophages and neutrophils at the injection site, with COF2, COF4 and COF5 attracting highest percentage of macrophages compared to DCs or neutrophils. COF1 attracted more DCs compared to other treatment groups (Fig. 3e, Supplementary Fig. 9a–c).

Amorphous COF with OVA results in a reduction in tumour growth and enhance OVA-specific T cell responses

Based on these in vitro results, which indicated the dependence of pro-inflammatory pathways in DCs on the degree of crystallinity, we aimed to investigate further if pro- or anti-inflammatory responses are generated due to the degree of crystallinity in vivo in melanoma mouse models. To evaluate the effect and significance of the degree of crystallinity of COFs on the development of immune responses in vivo, C57BL/6j mice were injected with B16F10 murine melanoma cells expressing OVA. COF1, COF3 and COF5 admixed with OVA, as a model antigen, were subcutaneously injected into the flank of the mice (contralaterally to the tumour site) on day 5. The tumour size was monitored for 20 days in these mice (Fig. 4a). This treatment of $COF1^+OVA$ resulted in a dramatic reduction in tumour growth compared to no treatment group, COF3 (semicrystalline COF), and COF5 (highest crystallinity) (Fig. 4b). Furthermore, the immune profiles of T cells were analysed by isolating cells in the tumour on day 20 (Supplementary Fig. 10). It was observed COF 1 (amorphous COF) with OVA formulation led to significant increases in T helper type 1 (Th1– $Tbet^+$ in $CD45^+CD4^+$) and T helper type 17 (Th17– $RoR\gamma t^+$ in $CD45^+CD4^+$), in tumour compared to no treatment, $COF3^+OVA$, and $COF5^+OVA$ treated mice (Fig. 4c, e). Additionally, significant increases in the number of activated Th1 ($Tbet^+CD44^+$ in $CD45^+CD4^+$) and activated Th17 ($RoR\gamma t^+CD44^+$ in $CD45^+CD4^+$) were observed in the tumour in mice treated with $COF1^+OVA$ as compared to other treatment groups (Fig. 4d, f). Notably, there was a decrease in the number of Treg cell population ($CD25^+Foxp3^+$ in $CD45^+CD4^+$) within tumour in $COF1^+OVA$ treated mice compared to no treatment control (Fig. 4g). Moreover, tumour infiltrating lymphocytes were characterized for OVA-specific $CD8^+$ T cells using H-2Kb tetramer loaded with OVA peptide (SIINFEKL peptide). COF^+OVA treatment enhanced the number of OVA-specific cytotoxic T cell 1 (Tc1, $Tbet^+OVA$ $tetramer^+$ in $CD45^+CD8^+$) and activated OVA-specific Tc1 ($CD44^+Tbet^+OVA$ $tetramer^+$ in $CD45^+CD8^+$), as compared to no treatment control (Fig. 4h, i). Within the tumour, no significant differences were observed in OVA-specific CD8 T effector cells (Tc17) and activated Tc17 in $COF1^+OVA$ and no treatment control (Supplementary Fig. 11a, b).

https://doi.org/10.1038/s41467-024-54227-9

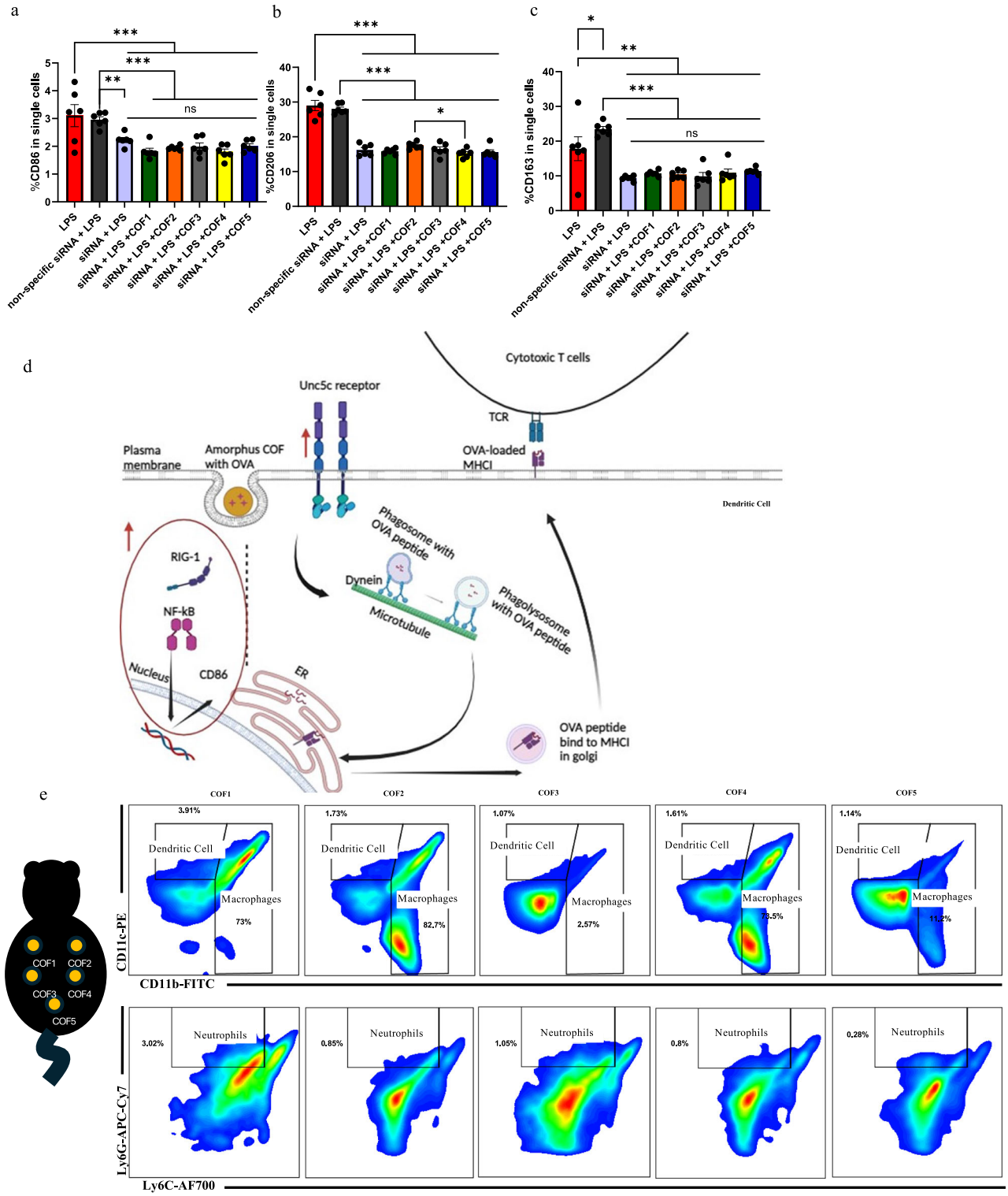

Fig. 3 | *Unc5c* plays a role in activation of bone marrow-derived dendritic cells treated with COFs, and in vivo amorphous COF1 accumulate more dendritic cells than crystalline counterpart. a–**c** No significant differences in the percentage of CD86, CD206, and CD163 when mouse DCs treated with COFs with LPS, in the presence of siRNA against *Unc5c*, in vitro (mean ± s.d, $n = 6$ biological replicate; one-way ANOVA test). **d** Associated between upregulation of RIG-I signalling pathway and *Unc5c* is shown. The RIG-I signalling pathway activates *NFkB* signalling and induces proinflammatory cytokines. *Unc5c* modulates microtubule function and vesicle transport in the cytoplasm, then can affect the interaction of DCs with cytotoxic T cells. Biorender file - Acharya, A. (2024) BioRender.com/y57h560. **e** COFs implanted in the same mouse were analysed for infiltrating innate cells, demonstrate that COF1 recruited higher percentages of dendritic cells and neutrophils as compared to the crystalline COFs, $n = 6$ mice per group, $^{*}p = 0.05$–0.01, $^{**}p < 0.01$, $^{***}p < 0.001$.

https://doi.org/10.1038/s41467-024-54227-9

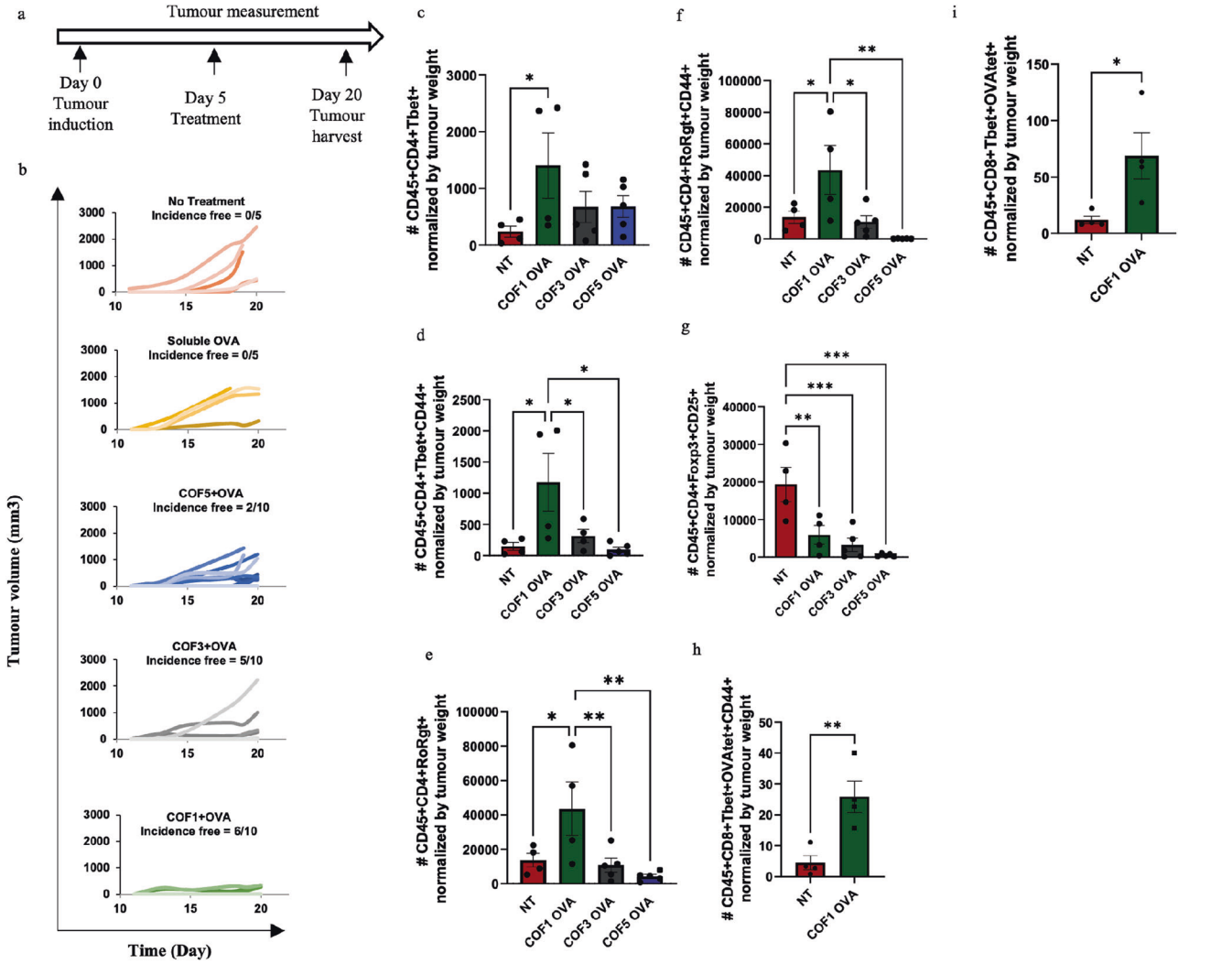

Fig. 4 | Anti-tumour responses, in terms of incidences of tumours and adaptive T cell responses are based on crystallinity of COFs. a Schema of in vivo tumour study. **b** Kinetics of tumour growth in vaccine treated mice, $n = 10$ for COFs with OVA, $n = 5$ for no treatment and soluble OVA. **c**–**f** Mice treated with COF1 with OVA had significantly higher number of Th1, activated Th1, Th17 and activated Th17, in tumours (mean ± s.d, $n = 4$–5 biological replicate, one-way unpaired ANOVA, Fisher LSD test). **g** Significantly lower number of Treg in tumours of mice treated with COF1 with OVA as compared to no treatment mice, (mean ± s.d, $n = 5$ or 4, one-way ANOVA Fisher LSD test). **h**, **i** The number of Tc1 cells and activated Tc1 cells in mice treated with COF1 OVA has significantly increased compared to the group that received no treatment, in vivo (mean ± s.d, $n = 4$–5 biological replicate, one-way ANOVA Fisher LSD test), $^{*}p = 0.05$–0.01, $^{**}p < 0.01$, $^{***}p < 0.001$.

Amorphous COF with TRP2 results in increased survival of melanoma-bearing mice

To test the fidelity of dependence of anti-tumour response on crystallinity of COFs, another mouse model of melanoma was tested. Specifically, first, subcutaneous tumours were generated with YUMM1.1 cancer cells (1,000,000 cells) with BRAFV600E mutation like those observed in human melanoma, in C57BL/6j mice. This cancer cell line is non-immunogenic and thus represents a tumour that shows significant challenges for immunotherapy generation. The mice were administered contralaterally to the tumours on day 5 subcutaneously with an endogenous and a clinically relevant antigen Tyrosinase-related protein-2 (TRP2) mixed with COF1, COF2, COF3, COF4 or COF5. The tumour growth curves were measured till mice were euthanized. It was observed that as compared to the no treatment control all the COFs delayed tumour growth in mice. However, there was no trend among the COFs themselves (Fig. 5a). Notably, when the frequency of activated $CD4^{+}$ and $CD8^{+}$ T cell population was measured using flow cytometry, it was observed that the amorphous COF1 was able to increase the activation population as compared to the crystalline COFs (Fig. 5b, Supplementary Fig. 12). These data suggest that although crystallinity by itself did not play a major role in modulating the non-immunogenic tumour growth responses, amorphous COF were able to better generate a pro-inflammatory response in the tumour as compared to the crystalline COFs.

Therefore, to further tease out if crystallinity indeed plays a role in tumour growth, mice were installed with lower number of cancer cells, to allow for immune response to develop. The growth of the tumours was measured in these mice. Tumour size in these mice was monitored every other day until it reached the maximum allowable size of 1.5 cm in any dimension, according to IACUC guidelines. Specifically, COF1 or COF5 mixed with TRP2 were injected contralaterally to the tumours on day 5. Survival comparison was performed by Kaplan–Meir test. The results showed an increased in survival of YUMM1.1 tumour-bearing mice treated with $COF1^{+}TRP2$ compared to $COF5^{+}TPP2$ and no treatment mice. After 105 days, 50% of mice treated with $COF1^{+}TRP2$ survived while only 16% of mice treated with COF5 and TRP2 survived, and no tumours were observed in these mice (Fig. 5c, d). To test if the mice retained the memory of the tumour, age-matched control mice and all surviving mice (tumour-free mice) treated with $COF1^{+}TRP2$ were rechallenge with YUMM1.1 cells

https://doi.org/10.1038/s41467-024-54227-9

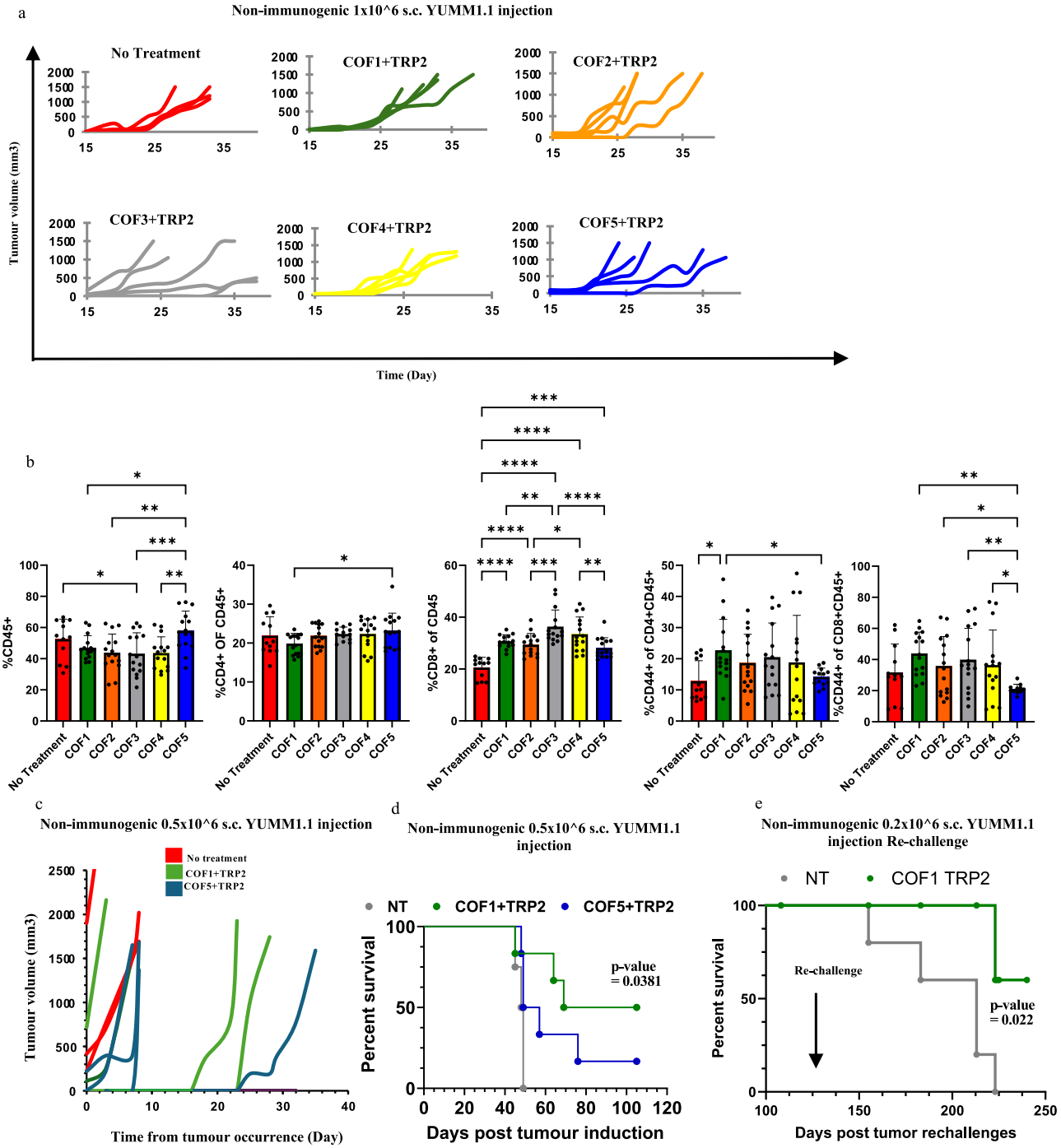

Fig. 5 | Non-immunogenic YUMM1.1 tumour responses, in terms of incidences of tumours and adaptive T cell responses are based on crystallinity of COFs. **a** Kinetics of tumour growth in vaccine treated mice, $n = 5$ per group, in a high tumour burden (1×10^6 cells). **b** Mice treated with amorphous COFs with TRP2 had significantly higher levels of activated (CD44 +) T cell responses as compared to the crystalline COFs, even though total frequency of the tumour infiltrating cells did not follow a pattern. (mean ± s.d, $n = 5$ biological replicate, $n = 10–13$ technical replicate per group, one-way unpaired ANOVA, Fisher LSD test). **c** Kinetics of tumour growth in COF1 with TRP2, or COF5 with TRP2 treated mice, $n = 6$ per group, in a medium tumour burden (0.5×10^6 cells). **d** Kaplan–Meier curve of survival YUMM1.1 melanoma in C57BL/6j in response to COF1 with TRP2, COF5 with TRP2, and PBS as a control ($n = 4–6$) in a medium tumour burden (0.5×10^6 cells). Logrank (Mantel–Cox) test for statistics. **e** Low tumour burden rechallenge study of mice that survived after being treated with COF1 with TRP2 and age-matched control ($n = 5$), Logrank (Mantel–Cox) test for statistics. The data are presented as the mean ± s.d, $^*p = 0.05–0.01$, $^{**}p < 0.01$, $^{***}p < 0.001$, $^{****}p < 0.0001$.

(200,000 cells) in the same flank as the initial inoculation. The tumour rechallenge was performed 108 days after the initial treatment (Fig. 5e). It was observed that the mice treated with COF1$^+$TRP2 had significantly extended survival compared to the age-matched control, thus demonstrating that the memory of this tumour was still retained, and the immune system was able to prevent their growth.

It is possible that the COFs when injected in vivo can have effects on different stromal cell types such as adipocytes, fibroblasts, endothelial cells and other innate and adaptive immune cells. The effect of varying crystallinity of COFs on other immune cell types such as neutrophils, primary macrophages, and adaptive T cells will be evaluated in future experiments. Furthermore, histology staining of main organs

(spleen, liver and kidney) of vaccinated mice was performed to evaluate COF toxicity in vivo. The result showed that there was no obvious inflammation in main organs of vaccinated mice with COFs (Supplementary Fig. 13). To understand the effect of COFs on liver and kidney toxicity, Alanine Aminotransferase Activity Assay (ALT) and Aspartate Aminotransferase Activity Assay (AST) performed on the serum of mice showed that there was no significant difference in ALT and AST level between controls (PBS – negative control, PLGA – biomaterial control) and COF1 and COF5 (Supplementary Fig. 14a, b). Additionally, TUNEL assay (shows apoptosis of cells), was performed to investigate in vivo toxicity in spleen, liver and kidney (Supplementary Fig. 15). From these studies, no obvious apoptosis as compared to the controls was observed in the organs isolated from COF treated mice.

Discussion

This study successfully synthesized COFs with variable crystallinity, and it was observed that there is a correlation between COF crystallinity and the activation of mouse and human dendritic cells in vitro and the generation of adaptive immune responses in mice. This reduction in activation of DCs due to increased crystallinity might be driven by genes such as *unc5c* which are important for the movement of DCs and upregulation of *RIG-I* signalling pathway. Additionally, the amorphous COFs were able to inhibit tumour growth in mouse models of melanoma, while highest crystalline COF were not as effective. Similar to COFs, other 2D nanomaterials, like graphene and graphene oxide (GO), have also shown immunological effects. For instance, myeloid-derived suppressor cells (MDSC) from experimental autoimmune encephalomyelitis (EAE) mice treated with GO films exhibited strong immunosuppressive effects on T lymphocytes[65]. These materials, including GO and crystalline graphene, have also been used for gene delivery[66], small molecule drug delivery[67], and cancer treatment[68–70]. Given the variability in crystallinity among such materials, further investigation is warranted to understand their immune effects. Moreover, the crystalline debris from other implant materials, such as ultra-high-molecular-weight polyethylene (UHMWPE)[71,72] and titanium alloys[73], should also be considered in future biomaterial design. Based on this study, understanding and harnessing the adjustable crystallinity of COF as a structure of vaccine can improve the generation of immune responses and enhance the efficacy of vaccine formulation. Therefore, the crystallinity of biomaterials should be considered while designing a pro- or anti-inflammatory biomaterial-based immunotherapeutic strategy.

Methods

Preparation of COFs

TABP-PDA COF was synthesized via a well-established[74] condensation reaction between terephthalaldehyde (PDA, CAS:623-27-8, Catalogue number:T0010, TCI) and 1,3,5-tris(4-aminophenyl) benzene (TAPB, 118727-34-7, Catalogue number:T2728, TCI) monomers. For a typical synthesis, 100 mg of TAPB (0.265 mmol) and 54.33 mg of PDA (0.397 mmol) were added to a 20 mL scintillation vial. 11.46 mL of 1,4-dioxane and mesitylene (4:1 v/v) were added to the vial which was sonicated thoroughly for 1 min to completely dissolve the contents. The vial was preheated to 70 °C before 5.45 mL of 10.5 M acetic acid was added to catalyse the reaction. The reaction time was varied in order to control the crystallinity of the final TAPB-PDA powder. After the specified reaction time, the COF powder was isolated by filtration and rinsed thoroughly with tetrahydrofuran and then methanol without allowing the product to dry at any point. The wet powder was transferred into custom paper bags followed by supercritical CO_2 drying to completely remove methanol while preserving the COF's crystallinity.

COF characterizations

Powder X-ray diffraction (PXRD) measurements were performed on a powder X-ray diffractometer (Malvern PANalytical Aeris) equipped with a PIXcel1D detector in a 2θ Bragg Brentano geometry. Dynamic light scattering (DLS) measurements were performed on a Malvern Zetasizer unit. Specifically, the as-synthesized TAPB-PDA COF powders were dispersed in deionized water at 1 mg/mL prior to DLS characterization. Scanning electron microscopy (SEM) was performed on a Helios 5 UX dual beam FIB-SEM operating at 20.00 kV. TAPB-PDA COF powders were transferred to carbon tape and coated with a 10 nm gold layer using a Desk II Denton Vacuum Inc. Sputterer for SEM characterization. Fourier-transform infrared (FT-IR) spectra of the as-synthesized COF powders were recorded using a Nicolet iS10 FT-IR spectrometer with 64 scans taken and averaged for each sample.

BMDC culture and human DC culture

Bone marrow-derived dendritic cells (BMDC) were generated from 6–8-week-old female C57BL/6j mice from Jackson Laboratory (Strain #:000664, Bar Harbour, ME), following the approved protocol by Arizona State University (protocol number 19-1688 R), using a modified 10-day procedure. Briefly, femur and tibia from the mice were isolated and kept in wash media (DMEM/F-12 (1:1) with L-glutamine (catalogue number:16777-255, VWR, Radnor, PA), 10% fetal bovine serum (catalogue number: F-0500-D, Atlanta Biologics, Flowery Branch, GA), and 1% penicillin-streptomycin (catalogue number: 15140122, VWR, Radnor, PA)). The bones were trimmed, and bone marrow was flushed out to create a homogenous suspension. Red blood cells (RBC) were lysed by centrifugation and incubation in 3 mL of 1X RBC lysis buffer (catalogue number:64010-00, biogem) for 5 min on ice. The cell suspension was centrifuged, washed with 7 mL wash media, and then resuspended in DC media (DMEM/F-12 with L-glutamine containing 10% fetal bovine serum, 1% sodium pyruvate (catalogue number: 12001-636, VWR, Radnor, PA), 1% non-essential amino acids (catalogue number: IC1681049, VWR, Radnor, PA), 1% penicillin-streptomycin, and 20 ng/mL GM-CSF (catalogue number: 10787-934, VWR, Radnor, PA)). The cells were seeded in a tissue culture-treated T-75 flask on Day 0. On Day 2, floating cells were collected, centrifuged, and resuspended in fresh media before being seeded on ultra-low attachment plates for an additional 7 days. The media was changed daily until Day 9. On Day 9, cells from the ultra-low attachment plates were resuspended, and 0.1×10^6 cells/well were seeded on suitable tissue culture plates for the desired experiments for 1 more day (until Day 10) before treatment. The cells in the tissue culture plates were utilized for further experiments/treatment on Day 10. The purity, immaturity, and yield of DCs were confirmed through immunofluorescence staining and flow cytometry. Human DCs were generated from human whole blood samples (gender unspecified, commercially purchased from BIOIVT). Human peripheral blood mononuclear cells (PBMC) from human blood isolated using Lymph prep solution (catalogue number: AXS-1114544, COSMO Bio USA). $CD14^+$ cells from human PBMCs using the MagCellect Human $CD14^+$ Cell Isolation Kit (catalogue number: MAG997, MAGH105, R&D systems-biotechne) isolated according to manufacture direction. Resuspend human $CD14^+$ cells at 1,000,000 cells/mL in Differentiation Media (catalogue number: CDK004, CellXVivo-biotechne). Add the cell suspension to the tissue culture flask Incubate the cells at 37 °C in a 5% CO2 atmosphere. On days 3 and 5, the media was changed by removing half of the media from the flask and replenishing with the same volume of fresh Differentiation Media. On day7, the cells in the tissue culture plates were utilized for further experiments/treatment.

Confocal images of COFs treated DCs

Bone marrow-derived dendritic cells (BMDCs) were isolated from 6–8 weeks old C57BL/6j mice from Jackson Laboratory (Strain #:000664, Bar Harbour, ME), using 10-day protocol (as describe in the previously method section). COF1-5 were labelled by rhodamine B isothiocyanate (RBITC, shown in MAGENTA), kept it overnight at room temperature on a rotisserie rotator. Before seeding cells in 24 well

plate, DCs were stained with 1,1-Dioctadecyl-3,3,3,3-tetramethylindodicarbocyanine (DiD) dye (shown in GREEN, catalogue number: 22033, AAT Bioquest). Then, BMDCs were seeded on a cover glass within 24 well plates, and they treated with COF1, COF2, COF3, COF4, and COF5 for 2 h at 37 °C. COF1 with cytochalasin D, COF3 with cytochalasin D, COF5 with cytochalasin D were used as controls. The working concentration of all COFs was 0.05 mg/ml. free dye was washed, and cells were fixed with 4% paraformaldehyde solution (PFA) for 15 min. Lastly, nucleus was stained with DAPI (shown in BLUE). The cells were imaged with scanning confocal microscope.

Induction of tumours and treatments

Female C57BL/6 J mice, aged 6–10 weeks, were procured from Jackson Laboratory (Strain #:000664, Bar Harbour, ME). All mice were housed in a pathogen-free environment at ambient temperature and humidity. All experiments were conducted in accordance with the Institutional Animal Care & Use Committee (IACUC) guidelines, approved under protocol numbers 19-1688 R at Arizona State University and 2023-0038 at Case Western Reserve University. For the B16F10-OVA melanoma model, B16F10 murine melanoma cells expressing ovalbumin[75,76] (250,000 cells, a generous gift from Dr. Louis Falo, University of Pittsburgh) were cultured in DMEM/F12 with L-glutamine, 10% fetal bovine serum, and 1% penicillin-streptomycin, at 37 °C in a 5% CO2 atmosphere. Prior to inoculation, the cells were detached using trypsin, centrifuged, and resuspended in 5 mL of culture media, with viability assessed by Trypan blue exclusion. The cells were then resuspended in sterile PBS, and 100 μL containing the cells were injected subcutaneously into the right flank of each mouse. Mice treated subcutaneously with 1 mg of microparticles containing endotoxin-free OVA (50 μg per formulation, OVA EndoFit, catalogue number: vac-pova, Invivo Gen) on the contralateral side of the tumour. Tumour growth was monitored every other day for 20 days using a digital calliper, and volume was calculated using the formula (longest length × narrowest length^2)/2 according to IACUC guidelines, the maximum allowable tumour size is 1.5 cm in any dimension. On day 20, mice were euthanized in accordance with the standard protocol for rodents using 100% carbon dioxide, with a chamber flow rate of 30–70% air change per minute. Then, tumours were collected. For YUMM1.1 tumour models, 6–8-week-old female mice were injected with 500,000 YUMM1.1 murine melanoma cells (a generous gift from Dr. David Klinke, West Virginia University). After tumours became palpable, mice were treated with COF1 or COF5 admixed with TRP2 (catalogue number:AS-64811, AnaSpace Inc), injected subcutaneously and contralaterally to the tumours. Mice weight and tumour growth were recorded throughout the experiment.

Endotoxin assay

The endotoxin levels in the synthesized COFs were measured using the Chromogenic LAL Endotoxin Assay Kit (catalogue number: A39552) from Thermo Fisher Scientific.

Culture of fibroblast and cytotoxicity assay

The cells, provided by Dr. Jeanne Wilson-Rawls lab, were incubated under standard conditions at 37 °C, in 5% carbon dioxide and at 95% humidity in Dulbecco's modified Eagles medium (DMEM, catalogue number: 30-2002, ATCC). The medium was mixed with 1% penicillin/streptomycin mix and 10% bovine calf serum as a supplement. The cells were sub-cultured using Trypsin-EDTA. The cells were grown to near 80% confluency, and trypsinized. After 2 h incubation with COFs (4 μg/ml and 0.8 μg/ml), cells were washed with 1xPBS and cultured for 24 h and then lysed using a radio-immunoprecipitation assay (RIPA) lysis (catalogue number: R0278, Sigma Aldrich). Fluorescence at 528 nm was measured and DNA concentration using the Quant-iT PicoGreen dsDNA Assay Kit (catalogue number: P7589, Thermo Fisher Scientific) was calculated.

Flow cytometry

Flow cytometry analysis was conducted using the Attune NXT system (BD Biosciences, BioLegend, Invitrogen, ThermoFisher, Waltham, MA, USA). Cells were stained with specific fluorescent antibodies in a 1% Fluorescent Activated Cell Sorting (FACS) buffer prepared with 0.001% bovine serum albumin, 0.5 M EDTA, and 0.0001% NaN3 in 1xPBS.

Bulk RNAseq

A PureLink RNA Mini Kit (12183018 A, 12183025) was used to isolate RNA from the treated DCs, 24 h post treatment. The KAPA mRNA HyperPrep Kit (KAPA KK8580) was utilized to generate mRNA sequencing libraries from total RNA. Magnetic oligo-dT beads were employed to capture mRNA, which was then sheared to approximately 300–350 bp using heat and magnesium. The 1st strand of the mRNA fragments underwent reverse transcription using random priming. To enable strand-specificity, the 2nd strand was generated with incorporated dUTP molecules. Subsequently, Illumina-compatible adaptors with unique indexes (IDT #00989130v2) were ligated on each sample individually. The adaptor-ligated molecules were then amplified for 10 cycles using KAPA's HIFI enzyme (KAPA KK2502). Fragment size was verified to be 450–500 bp on an Agilent Tapestation, and quantification was performed with a Qubit before multiplex pooling. The pooled samples were sequenced on the Illumina NovaSeq6000 platform with a 2x150 flow cell at the University of Colorado Anschutz Medical Campus Genomics Core facility.

Animal dosing, H&E staining and TUNEL assay

Female C57BL/6 J mice between 6 weeks and 10 weeks old were purchased from Jackson Laboratory (Strain #:000664, Bar Harbour, ME. Mice were housed in cages with 3 mice per cage, all mice were housed in a pathogen-free environment at ambient temperature and humidity. Mice were subcutaneously injected with 1 mg of PLGA, COF1 and COF5 and PBS as a control group at day 0. On day 30, main organs (liver, kidney, and spleen) were collected. H&E staining (catalogue number: MER47991GL, Mercedes Scientific, catalogue number: E511-25, Thermo Fisher Scientific) and TUNEL assay (catalogue number: S7100, Millipore Sigma) were performed according to manufacture direction.

siRNA gene knock-down

Bone marrow-derived dendritic cells were cultured with siRNA (catalogue number: A-046955-13-0005, horizon discovery, Supplementary Tabel 2) against *Unc5c* (1 μM) and lipofectamine (as a transfection reagent) for 72 h and then COFs and LPS were added to the culture for 2 h. After 24 h of further culture with internalized COFs, flow cytometry was performed to determine the activation phenotype of DCs.

The ALT and AST assays

The ALT (catalogue number: 700260, Cayman) and AST (catalogue number: 701640, Cayman) assays were performed following the manufacturer's instruction (Cayman Chemical). Female C57BL/6 J mice between 6 weeks and 10 weeks old were purchased from Jackson Laboratory (Strain #:000664, Bar Harbour, ME. Mice were housed in cages with 3 mice per cage, all mice were housed in a pathogen-free environment at ambient temperature and humidity. For ALT assay, substrate (L-alanine), cofactor (NADH and LDH), initiator (α-ketoglutarate) solutions were prepared using the reagents and assay buffer (100 mM Tris-HCl, 10 mM NaHCO3, 0.1 mM pyridoxal-5'-phosphate, and 0.01% NaN3, pH = 7.8) in the kit. Blood samples from mice treated with PBS, PLGA, COF1, or COF5 were centrifuged at 2000 g for 15 min and the serum was used in the assay without dilution. In a 96-well plate, 150 μL substrate, 20 μL cofactor, and 20 μL serum sample (assay buffer for background and porcine heart ALT for positive control, respectively) were added to wells and the plate was incubated at 37 °C for 15 min. Upon the addition of initiator, the plate was shaken for 20 s on a microplate reader and the absorbance at 340 nm was measured every

minute for 15 min. A linear fitting (least squares method) of Abs340nm vs time (min) was conducted and the slopes of the fitting were used to represent ALT activity. AST assays were conducted similarly with aspartate as the substrate.

Statistics

Data are expressed as average ± standard deviation (mean ± s.d.) or average ± standard error (mean ± SEM.). Comparisons between multiple treatment groups were performed using one-way ANOVA with Fisher's LSD test and *p*-values of smaller than 0.05 were considered statistically significant (GraphPad Prism Software 6.0, San Diego, CA).

Reporting summary

Further information on research design is available in the Nature Portfolio Reporting Summary linked to this article.

Data availability

Source data are provided in this paper. All data are included in the Supplementary Information or available from the authors, as are unique reagents used in this Article. The raw numbers for charts and graphs are available in the Source Data file whenever possible. The RNAseq data have been deposited in NCBI under the accession code: PRJNA1166734 (https://www.ncbi.nlm.nih.gov/bioproject/1166734). Source data are provided with this paper.

References

1. Moon, J. J. et al. Interbilayer-crosslinked multilamellar vesicles as synthetic vaccines for potent humoral and cellular immune responses. *Nat. Mater.* **10**, 243–251 (2011).
2. Kuai, R., Ochyl, L. J., Bahjat, K. S., Schwendeman, A. & Moon, J. J. Designer vaccine nanodiscs for personalized cancer immunotherapy. *Physiol. Behav.* **176**, 139–148 (2017).
3. Allen, R., Chizari, S., Ma, J. A., Raychaudhuri, S. & Lewis, J. S. Combinatorial, microparticle-based delivery of immune modulators reprograms the dendritic cell phenotype and promotes remission of collagen-induced arthritis in mice. *ACS Appl. Bio Mater.* **2**, 2388–2404 (2019).
4. Acharya, A. P. et al. Localized multi-component delivery platform generates local and systemic anti-tumor immunity. *Adv. Funct. Mater.* **27**, 1604366 (2017).
5. Damo, M., Wilson, D. S., Simeoni, E. & Hubbell, J. A. TLR-3 stimulation improves anti-tumor immunity elicited by dendritic cell exosome-based vaccines in a murine model of melanoma. *Sci. Rep.* **5**, 1–15 (2015).
6. Costa Clemens, S. A. et al. Heterologous versus homologous COVID-19 booster vaccination in previous recipients of two doses of CoronaVac COVID-19 vaccine in Brazil (RHH-001): a phase 4, non-inferiority, single blind, randomised study. *Lancet* **399**, 521–529 (2022).
7. Xia, S. et al. Safety and immunogenicity of an inactivated SARS-CoV-2 vaccine, BBIBP-CorV: a randomised, double-blind, placebo-controlled, phase 1/2 trial. *Lancet Infect. Dis.* **21**, 39–51 (2021).
8. Yousefpour, P., Ni, K. & Irvine, D. J. Targeted modulation of immune cells and tissues using engineered biomaterials. *Nat. Rev. Bioeng.* **1**, 107–124 (2023).
9. Zolnik, B. S., González-Fernández, Á., Sadrieh, N. & Dobrovolskaia, M. A. Minireview: nanoparticles and the immune system. *Endocrinology* **151**, 458–465 (2010).
10. Liu, J., Liu, Z., Pang, Y. & Zhou, H. The interaction between nanoparticles and immune system: application in the treatment of inflammatory diseases. *J. Nanobiotechnol.* **20**, 1–25 (2022).
11. Chen, Z., Yue, Z., Wang, R., Yang, K. & Li, S. Nanomaterials: a powerful tool for tumor immunotherapy. *Front. Immunol.* **13**, 1–25 (2022).
12. Panyam, J. & Labhasetwar, V. Biodegradable nanoparticles for drug and gene delivery to cells and tissue. *Adv. Drug Deliv. Rev.* **64**, 61–71 (2012).
13. Zolnik, B. S. & Sadrieh, N. Regulatory perspective on the importance of ADME assessment of nanoscale material containing drugs. *Adv. Drug Deliv. Rev.* **61**, 422–427 (2009).
14. Mundargi, R. C., Babu, V. R., Rangaswamy, V., Patel, P. & Aminabhavi, T. M. Nano/micro technologies for delivering macromolecular therapeutics using poly(d,l-lactide-co-glycolide) and its derivatives. *J. Control. Release* **125**, 193–209 (2008).
15. Food and Drug Administration. Liposome drug products - guidance for industry. *Pharm. Qual.* Revision **1**, 1–13 (2015).
16. Murali, A., Lokhande, G., Deo, K. A., Brokesh, A. & Gaharwar, A. K. Emerging 2D nanomaterials for biomedical applications. *Mater. Today* **50**, 276–302 (2021).
17. Hossain, N., Chowdhury, M. A., Sultana, S. & Nandee, R. Scope of 2D materials for immune response-a review. *Results Eng.* **14**, 100413 (2022).
18. Nguyen, E. P., De Carvalho Castro Silva, C. & Merkoçi, A. Recent advancement in biomedical applications on the surface of two-dimensional materials: From biosensing to tissue engineering. *Nanoscale* **12**, 19043–19067 (2020).
19. Zhang, X. et al. Cu2+embedded three-dimensional covalent organic framework for multiple ROS-based cancer immunotherapy. *ACS Appl. Mater. Interfaces* **14**, 30618–30625 (2022).
20. Sun, M. et al. Bioorthogonal-activated in situ vaccine mediated by a COF-based catalytic platform for potent cancer immunotherapy. *J. Am. Chem. Soc.* **145**, 5330–5341 (2023).
21. Lu, Z. et al. Porphyrin-based covalent organic framework for imaging-guided cancer combinatorial immuno-sonodynamic therapy. *Adv. Funct. Mater.* **32**, 1–15 (2022).
22. Singh, N. et al. Covalent organic framework nanomedicines: biocompatibility for advanced nanocarriers and cancer theranostics applications. *Bioact. Mater.* **21**, 358–380 (2023).
23. Yuan, F. et al. An erythrocyte membrane-camouflaged fluorescent covalent organic framework for starving/nitric oxide/immunotherapy of triple-negative breast cancer. *Chem. Sci.* **00**, 1–11 (2023).
24. Kagan, V. E. et al. Carbon nanotubes degraded by neutrophil myeloperoxidase induce less pulmonary inflammation. *Nat. Nanotechnol.* **5**, 354–359 (2010).
25. Gao, P. et al. A COF-based nanoplatform for highly efficient cancer diagnosis, photodynamic therapy and prognosis. *Chem. Sci.* **11**, 6882–6888 (2020).
26. Reddy, S. T. et al. Exploiting lymphatic transport and complement activation in nanoparticle vaccines. *Nat. Biotechnol.* **25**, 1159–1164 (2007).
27. HogenEsch, H., O'Hagan, D. T. & Fox, C. B. Optimizing the utilization of aluminum adjuvants in vaccines: you might just get what you want. *npj Vaccines* **3**, 1–11 (2018).
28. Kool, M. et al. Alum adjuvant boosts adaptive immunity by inducing uric acid and activating inflammatory dendritic cells. *J. Exp. Med.* **205**, 869–882 (2008).
29. Purwada, A., Roy, K. & Singh, A. Engineering vaccines and niches for immune modulation. *Acta Biomater.* **10**, 1728–1740 (2014).
30. Hornung, V. et al. Silica crystals and aluminum salts activate the NALP3 inflammasome through phagosomal destabilization. *Nat. Immunol.* **9**, 847–856 (2008).
31. Swanson, K. V., Deng, M. & Ting, J. P. Y. The NLRP3 inflammasome: molecular activation and regulation to therapeutics. *Nat. Rev. Immunol.* **19**, 477–489 (2019).
32. Sun, B. et al. Engineering an effective immune adjuvant by designed control of shape and crystallinity of aluminum oxyhydroxide nanoparticles. *ACS Nano* **7**, 10834–10849 (2013).
33. Jensen-Jarolim, E. et al. State-of-the-art in marketed adjuvants and formulations in Allergen Immunotherapy: A position paper of the European Academy of Allergy and Clinical Immunology (EAACI). *Allergy Eur. J. Allergy Clin. Immunol.* **75**, 746–760 (2020).

34. Leuthard, D. S. et al. Microcrystalline tyrosine and aluminum as adjuvants in allergen-specific immunotherapy protect from IgE-mediated reactivity in mouse models and act independently of inflammasome and TLR signaling. *J. Immunol.* **200**, 3151–3159 (2018).
35. Williams, G. R. et al. Immunity induced by a broad class of inorganic crystalline materials is directly controlled by their chemistry. *J. Exp. Med.* **211**, 1019–1025 (2014).
36. Gower, L. B. Biomimetic model systems for investigating the amorphous precursor pathway and its role in biomineralization. *Chem. Rev.* **108**, 4551–4627 (2008).
37. Rydén, L. et al. Inflammatory cell response to ultra-thin amorphous and crystalline hydroxyapatite surfaces. *J. Mater. Sci. Mater. Med.* **28**, 9 (2017).
38. Kołbuk, D., Ciechomska, M., Jeznach, O. & Sajkiewicz, P. Effect of crystallinity and related surface properties on gene expression of primary fibroblasts. *RSC Adv.* **12**, 4016–4028 (2022).
39. Montoya, C. et al. On the road to smart biomaterials for bone research: definitions, concepts, advances, and outlook. *Bone Res.* **9**, 12 (2021).
40. Li, Y., Chen, W., Xing, G., Jiang, D. & Chen, L. New synthetic strategies toward covalent organic frameworks. *Chem. Soc. Rev.* **49**, 2852–2868 (2020).
41. Matsumoto, M. et al. Rapid, low temperature formation of imine-linked covalent organic frameworks catalyzed by metal triflates. *J. Am. Chem. Soc.* **139**, 4999–5002 (2017).
42. Biswal, B. P. et al. Mechanochemical synthesis of chemically stable isoreticular covalent organic frameworks. *J. Am. Chem. Soc.* **135**, 5328–5331 (2013).
43. Bhunia, S., Deo, K. A. & Gaharwar, A. K. 2D covalent organic frameworks for biomedical applications. *Adv. Funct. Mater.* **30**, 1–27 (2020).
44. Bhunia, S., Jaiswal, M. K., Singh, K. A., Deo, K. A. & Gaharwar, A. K. 2D covalent organic framework direct osteogenic differentiation of stem cells. *Adv. Healthc. Mater.* **11**, 1–11 (2022).
45. Uribe-Romo, F. J. et al. A crystalline imine-linked 3-D porous covalent organic framework. *J. Am. Chem. Soc.* **131**, 4570–4571 (2009).
46. Esrafili, A., Wagner, A., Inamdar, S. & Acharya, A. P. Covalent organic frameworks for biomedical applications. *Adv. Healthc. Mater.* **10**, 2002090 (2021).
47. Qian, C. et al. Imine and imine-derived linkages in two-dimensional covalent organic frameworks. *Nat. Rev. Chem.* **6**, 881–898 (2022).
48. Martínez-Abadía, M. & Mateo-Alonso, A. Structural approaches to control interlayer interactions in 2D covalent organic frameworks. *Adv. Mater.* **32**, 1–22 (2020).
49. Galgani, M. et al. Cyclic AMP modulates the functional plasticity of immature dendritic cells by inhibiting Src-like kinases through protein kinase A-mediated signaling. *J. Biol. Chem.* **279**, 32507–32514 (2004).
50. Chinn, A. M. & Insel, P. A. Cyclic AMP in dendritic cells: a novel potential target for disease-modifying agents in asthma and other allergic disorders. *Br. J. Pharmacol.* **177**, 3363–3377 (2020).
51. Wu, J., Wang, G., He, B., Chen, X. & An, Y. Methylation of the UNC5C gene and its protein expression in colorectal cancer. *Tumor Biol.* **39**, 1010428317697564 (2017).
52. Chen, G. et al. Netrin-1 receptor UNC5C cleavage by active-secretase enhances neurodegeneration, promoting Alzheimer's disease pathologies. *Sci. Adv.* **7**, 1–16 (2021).
53. Malemud, C. J. Inhibition of MMPs and ADAM/ADAMTS. *Biochem. Pharmacol.* **165**, 33–40 (2019).
54. Zhang, L. et al. Selenium regulation of the immune function of dendritic cells in mice through the ERK, Akt and RhoA/ROCK pathways. *Biol. Trace Elem. Res.* **199**, 3360–3370 (2021).
55. Esser, C., Rannug, A. & Stockinger, B. The aryl hydrocarbon receptor in immunity. *Trends Immunol.* **30**, 447–454 (2009).
56. Nile, R. et al. Crystallization behavior of semicrystalline polymers characterized by an in situ fluorescence technique and its sensing mechanism. *Macromol. Chem. Phys.* **224**, 1–12 (2023).
57. Beltrán, F. R. et al. Water-induced structural changes in poly(lactic acid) and PLLA-clay nanocomposites. *Polymer* **107**, 211–222 (2016).
58. Righetti, M. C., Gazzano, M., Di Lorenzo, M. L. & Androsch, R. Enthalpy of melting of α′- and α-crystals of poly(L-lactic acid). *Eur. Polym. J.* **70**, 215–220 (2015).
59. MK Wetzel-Smith, et al. A rare mutation in UNC5C predisposes to Alzheimer's disease and increases neuronal cell death. *Nat. Med.* **20**, 1452–7 (2014).
60. Li, Q. et al. The role of UNC5C in Alzheimer's disease. *Ann. Transl. Med.* **6**, 178–178 (2018).
61. Iurescia, S., Fioretti, D. & Rinaldi, M. The innate immune signalling pathways: Turning RIG-I sensor activation against cancer. *Cancers (Basel)* **12**, 1–26 (2020).
62. Zhang, H. X. et al. Rig-I regulates NF-κB activity through binding to Nf-κb1 3′-UTR mRNA. *Proc. Natl. Acad. Sci. USA* **110**, 6459–6464 (2013).
63. Connors, J. et al. Aging alters antiviral signaling pathways resulting in functional impairment in innate immunity in response to pattern recognition receptor agonists. *GeroScience* **44**, 2555–2572 (2022).
64. Mylvaganam, S., Freeman, S. A. & Grinstein, S. The cytoskeleton in phagocytosis and macropinocytosis. *Curr. Biol.* **31**, R619–R632 (2021).
65. Camacho-toledano, C. et al. Graphene oxide films as a novel tool for the modulation of myeloid-derived suppressor cell activity in the context of multiple sclerosis. https://doi.org/10.1039/d3nr05351b (2024).
66. Feng, L., Zhang, S. & Liu, Z. Graphene based gene transfection. *Nanoscale* **3**, 1252–1257 (2011).
67. Yang, X. et al. High-efficiency loading and controlled release of doxorubicin hydrochloride on graphene oxide. *J. Phys. Chem. C* **112**, 17554–17558 (2008).
68. Sun, X. et al. Nano-graphene oxide for cellular imaging and drug delivery. *Nano Res.* **1**, 203–212 (2008).
69. Chung, C. et al. Biomedical applications of graphene and graphene oxide. *Acc. Chem. Res.* **46**, 2211–2224 (2013).
70. Liu, Z., Robinson, J. T., Sun, X. & Dai, H. PEGylated nanographene oxide for delivery of water-insoluble cancer drugs. *J. Am. Chem. Soc.* **130**, 10876–10877 (2008).
71. Hussain, M. et al. Ultra-high-molecular-weight-polyethylene (UHMWPE) as a promising polymer material for biomedical applications: a concise review. *Polymers (Basel)* **12**, 1–28 (2020).
72. Hassanein, N., Bougherara, H. & Amleh, A. In- vitro evaluation of the bioactivity and the biocompatibility of a novel coated UHMWPE biomaterial for biomedical applications. *J. Mech. Behav. Biomed. Mater.* **101**, 103409 (2020).
73. Elias, C. N., Fernandes, D. J., De Souza, F. M., Monteiro, E. D. S. & De Biasi, R. S. Mechanical and clinical properties of titanium and titanium-based alloys (Ti G2, Ti G4 cold worked nanostructured and Ti G5) for biomedical applications. *J. Mater. Res. Technol.* **8**, 1060–1069 (2019).
74. Feriante, C. et al. New mechanistic insights into the formation of imine-linked two-dimensional covalent organic frameworks. *J. Am. Chem. Soc.* **142**, 18637–18644 (2020).
75. Falo, D. & Thompson, K. Targeting antigen into the phagocytic pathway in vivo induces protective tumour immunity. *Nat. Med.* **1**, 649–53 (1995).
76. Celluzzi, C. M. & Falo, L. D. Epidermal dendritic cells induce potent antigen-specific CTL-mediated immunity. *J. Invest. Dermatol.* **108**, 716–720 (1997).

Acknowledgements

The authors acknowledge funding from National Institute of Health 1 R01 AI155907-01 and R01AR078343 to A.P.A. and from ACS Petroleum

Research Fund FP00030762 to K.J. for supporting this study. The authors also acknowledge support from the NASA Space Technology Graduate Research Opportunities (NSTGRO) fellowship programme (for Richard Nile; Grant 80NSSC21K1274). This research was supported by the Tissue Resources Core Facility of the Comprehensive Cancer Centre of Case Western Reserve University and University Hospitals of Cleveland (P30 CA43703). Alo, the authors thank Dr. Jeanne Wilson-Rawls for providing NIH3T3 cells for testing cytotoxicity and Khaled Nafee and Brian Ridenour for their partial contribution to the COF synthesis. The authors also acknowledge NIH Shared Instrumentation Grant (S10-NIH OD021559) of the Case Comprehensive Cancer Centre Cytometry & Microscopy.

Author contributions

A.E. and A.T. designed the study, performed experiments, and wrote the manuscript, M.M.C.S.J., J.K., A.P.S., S.J.S., Y.W.S., T.K.H. and K.L. performed in vivo experiments, G.N. and X.T. synthesized COFs, A.M. and B.K. performed H&E and TUNEL assay, W.S., M.D. performed in vitro assays, H.Q. performed siRNA experiments, and S.P., J.H., K.J. and A.P.A. provided guidance, and wrote the manuscript.

Competing interests

The authors declare no competing interests.

Additional information

Supplementary information The online version contains supplementary material available at https://doi.org/10.1038/s41467-024-54227-9.

Correspondence and requests for materials should be addressed to Abhinav P. Acharya.

Peer review information *Nature Communications* thanks Guiyang Zhang and the other anonymous reviewer(s) for their contribution to the peer review of this work. A peer review file is available.